Combining experiment and optical simulation in coherent X-ray nanobeam characterization of Si/SiGe semiconductor heterostructures

J. A. Tilka, J. Park, Y. Ahn, A. Pateras, K. C. Sampson, D. E. Savage, J. R. Prance, C. B. Simmons, S. N. Coppersmith, M. A. Eriksson, M. G. Lagally, M. V. Holt, and P. G. Evans

---

Articles you may be interested in

High-resolution x-ray diffraction investigation of relaxation and dislocations in SiGe layers grown on (001), (011), and (111) Si substrates
J. Appl. Phys. **109**, 123714 (2011); 10.1063/1.3597828

Growth mechanism of Si nanowhiskers and SiGe heterostructures in Si nanowhiskers: X-ray scattering and electron microscopy investigations
Appl. Phys. Lett. **89**, 153129 (2006); 10.1063/1.2360225

Analysis of x-ray diffraction as a probe of interdiffusion in Si/SiGe heterostructures
J. Appl. Phys. **94**, 1557 (2003); 10.1063/1.1589600

Si/SiGe modulation-doped heterostructures grown on silicon-on-insulator substrates for high-mobility two-dimensional electron gases
Appl. Phys. Lett. **79**, 2031 (2001); 10.1063/1.1400769

Diffuse x-ray scattering of misfit dislocations at Si $_{1-x}$ Ge $_x$ /Si interfaces by triple crystal diffractometry
J. Appl. Phys. **82**, 1172 (1997); 10.1063/1.365885

Combining experiment and optical simulation in coherent X-ray nanobeam characterization of Si/SiGe semiconductor heterostructures

J. A. Tilka,[1] J. Park,[1] Y. Ahn,[1] A. Pateras,[1] K. C. Sampson,[1] D. E. Savage,[1] J. R. Prance,[2] C. B. Simmons,[2] S. N. Coppersmith,[2] M. A. Eriksson,[2] M. G. Lagally,[1] M. V. Holt,[3] and P. G. Evans[1,a)]

[1]*Department of Materials Science and Engineering, University of Wisconsin-Madison, Madison, Wisconsin 53706, USA*
[2]*Department of Physics, University of Wisconsin-Madison, Madison, Wisconsin 53706, USA*
[3]*Center for Nanoscale Materials, Argonne National Laboratory, Argonne, Illinois 60439, USA*

The highly coherent and tightly focused x-ray beams produced by hard x-ray light sources enable the nanoscale characterization of the structure of electronic materials but are accompanied by significant challenges in the interpretation of diffraction and scattering patterns. X-ray nanobeams exhibit optical coherence combined with a large angular divergence introduced by the x-ray focusing optics. The scattering of nanofocused x-ray beams from intricate semiconductor heterostructures produces a complex distribution of scattered intensity. We report here an extension of coherent x-ray optical simulations of convergent x-ray beam diffraction patterns to arbitrary x-ray incident angles to allow the nanobeam diffraction patterns of complex heterostructures to be simulated faithfully. These methods are used to extract the misorientation of lattice planes and the strain of individual layers from synchrotron x-ray nanobeam diffraction patterns of Si/SiGe heterostructures relevant to applications in quantum electronic devices. The systematic interpretation of nanobeam diffraction patterns from semiconductor heterostructures presents a new opportunity in characterizing and ultimately designing electronic materials. *Published by AIP Publishing.*
[http://dx.doi.org/10.1063/1.4955043]

I. INTRODUCTION

A new generation of x-ray scattering and diffraction techniques based on the use of highly coherent tightly focused x-ray beams from hard x-ray light sources has created opportunities to better characterize the nanoscale structure of semiconductors but simultaneously poses significant challenges in the quantitative interpretation of diffraction data. Tightly focused x-ray beams promise to allow the characterization of the distribution of strain, composition, and lattice orientation at length scales of tens of nanometers. Such scales are relevant to fundamental physical processes in the formation and interaction of structural defects during epitaxy,[1] the patterning of surface features via self-assembly,[2,3] and the creation of semiconductor devices.[4] Control of the biaxial distortion of Si is important because strain induces interface band offsets and lowers the degeneracy of the conduction band minima of Si.[5,6] A biaxially strained thin film of Si grown between relaxed SiGe layers breaks this degeneracy and further forms a Si quantum well (QW) layer applicable to quantum devices but is accompanied by structural effects associated with plastic relaxation.[1,6–8] With control over the lateral variation of strain, it becomes possible to incorporate elastic deformation into the design of quantum devices in new ways, including the possibility of creating devices in which quantum wells are defined completely by strain.[9] Understanding and control on the mesoscopic nanometer-to-micron scale is crucial in Si/SiGe and other semiconductor heterostructures and thus has been an important goal of advanced structural characterization techniques.

In this work, we report the development of methods for the quantitative simulation of coherent x-ray nanobeam diffraction and the analysis of nanodiffraction intensity data acquired from Si/SiGe heterostructures. In the past, x-ray characterization of thin films and superlattices using nominally parallel incident x-ray beams has had a transformative impact on the development of semiconductor heterostructures. The parallel-beam approach is based on an analysis in which the incident x-ray beam can be approximated as a plane wave, the interpretation of heterostructure and superlattice diffraction intensity distributions is well-known, and there is a straightforward and effective mapping between the angular distribution of diffracted intensity and the structure of the sample.[10,11] The highly coherent and convergent x-rays produced by nanofocusing optics complicate the well-established parallel beam picture and provide novel opportunities.

Significant progress has already been made in understanding how structural information is encoded in coherent x-ray diffraction patterns acquired with highly convergent hard x-ray beams from nanocrystals and two-dimensional structures. The diffraction problem can be considered using the general framework of coherent diffraction imaging techniques.[12–14] Computational methods are used to retrieve the illumination function[15,16] and to form the images of projections of the strain along specific crystallographic directions or dislocation strain fields.[17,18] Intricate semiconductor heterostructures face challenges associated with the reciprocal-space

a)Electronic mail: pgevans@wisc.edu

overlap of scattering features from individual layers and can be analyzed using computational methods simulating and interpreting the experimental results. Here, we use wave-optics simulations to obtain the focused beam produced by a Fresnel-zone plate focusing optic and use kinematic diffraction methods to model the coherent x-ray Bragg diffraction patterns from a complex heterostructure illuminated at arbitrary angles of incidence.

Previous studies of the distortion of semiconductor structures using x-ray nanobeams have probed a variety of structural issues but have not yet closed the gap between experiment and simulation of complex heterostructures. Bragg projection ptychography analysis of focused x-ray nanobeam diffraction patterns has provided high-resolution imaging of tilts and strains in silicon-on-insulator test structures and in prototype field-effect transistor channels.[19,20] Similar lattice rotation and distortion effects are observed in ptychography studies of III-V heterostructures.[21] Nanobeam diffraction studies of Si/SiGe structures show that the lattice of the Si QW is distorted by the relaxation of the SiGe substrate[22] and by stresses imparted on the semiconductor through interfaces with metal electrodes.[23] Other nanobeam diffraction studies have probed the strain distribution over lateral lengths scales of microns in Ge microstripes,[24] hetero-epitaxial Ge,[25] and SiGe via rapid mapping techniques.[26,27] In semiconductor nanotechnology, x-ray nanobeam techniques provide insight into the distortion of thin semiconductor substrates by self-assembled quantum dots,[28,29] stresses arising from the freestanding SiGe membranes transferred to a new host substrate,[30] and the effect of patterning the silicon substrate on dislocation formation.[31] Advanced analysis techniques will permit the characterization of multilayers, quantum wells, and other intricate heterostructures. Here, we consider in detail the nanodiffraction characterization of the Si/SiGe heterostructure shown in Fig. 1(a), and we demonstrate that the gap between experiment and simulation can be closed.

II. EXPERIMENTAL METHODS

Nanobeam diffraction patterns were acquired with the Hard X-ray Nanoprobe of the Advanced Photon Source at Argonne National Laboratory. The optical configuration of the x-ray measurement is illustrated in Fig. 1(b). An incident x-ray beam with a photon energy of 10 keV, selected by a two-bounce Si (111) monochromator, was focused to a measured spot size of approximately 50 nm full width at half-maximum (FWHM) at the sample. The focusing optics consisted of a 160 μm-diameter Fresnel zone plate with a 60 μm-diameter center stop. The focusing introduced an overall effective beam divergence of 0.24°. The sample was placed at the first order focus of the zone plate, and radiation focused to higher orders was blocked by an order sorting aperture (OSA). The incident angle of the x-rays with respect to the heterostructure was set using the orientation of the sample, as indicated in Fig. 1(b). The intensity distribution of scattered x-rays was recorded using a two-dimensional charge coupled device (CCD) detector with a pixel size of 13 μm.
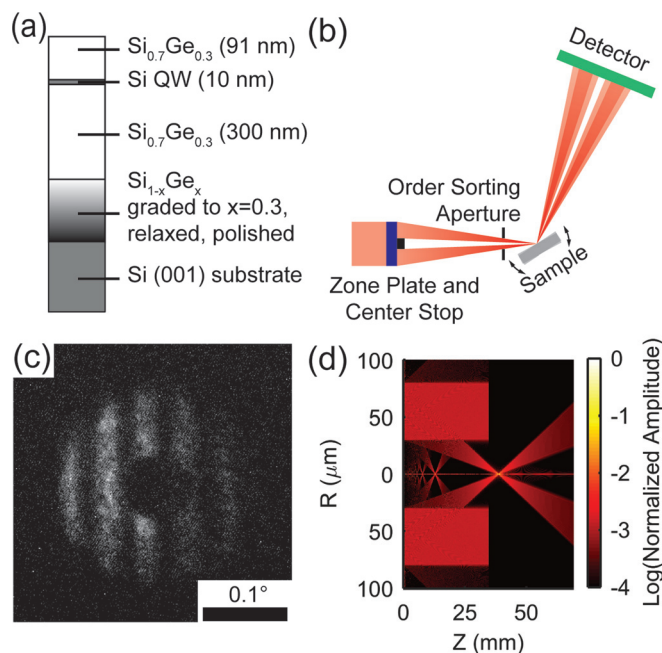

FIG. 1. (a) Schematic cross section of the Si/SiGe heterostructure grown on a graded SiGe layer on an (001)-oriented Si single crystal substrate. (b) Focused x-ray nanodiffraction geometry using Fresnel zone plate x-ray focusing optics and a two-dimensional CCD detector. Arrows indicate the direction of the sample rotation used to vary the x-ray incident angle. (c) Focused x-ray nanobeam diffraction pattern acquired at an angle close to the Bragg condition of the (004) reflection of the strained-Si QW. Intensity fringes visible as vertical stripes on the diffraction pattern originate from the thickness of the 91 nm-thick top SiGe layer. (d) Radial slice of the three-dimensional simulated wave front propagating from the zone plate to an axial position past the focus. Cylindrical coordinates Z and R correspond to the distance along the direction between the zone plate and the sample and the distance from the optical axis, respectively.

The Si/SiGe heterostructure was epitaxially grown using ultrahigh vacuum chemical vapor deposition. A several-μm-thick Si$_{1-x}$Ge$_x$ layer in which the Ge concentration is graded linearly from x = 0 to 0.3 was grown on a (001) Si substrate. During growth, the Si$_{1-x}$Ge$_x$ layer was relaxed forming a network of dislocations arranged in the characteristic cross-hatch pattern.[7] The Si/SiGe heterostructure (91 nm Si$_{0.7}$Ge$_{0.3}$, 10 nm strained-Si QW, 300 nm Si$_{0.7}$Ge$_{0.3}$, 5 nm Si cap layer) was then grown as shown in Fig. 1(a). A biaxial in-plane tensile strain with a magnitude of approximately 1% is induced in the Si QW by epitaxial growth on the relaxed Si$_{0.7}$Ge$_{0.3}$ layer.

III. COHERENT DIFFRACTION SIMULATION AND ANALYSIS METHODS

Diffraction experiments using highly coherent nanobeams produce a complex distribution of scattered intensity. A representative nanobeam diffraction pattern acquired from the Si/SiGe heterostructure is shown in Fig. 1(c), acquired at an incident angle at which the diffraction pattern exhibits features arising from the (004) Bragg reflection of the strained-Si QW. The incident angle of Fig. 1(c), $\theta = 27.49°$, corresponds to a nominal wavevector $q_z = 4.68$ Å^{-1} at the photon energy of this experiment. As discussed in detail below, the divergence introduced by the zone plate focusing optics results in the distribution of intensity in the focused x-ray beam of a range of incident angles, a wavevector range

$\Delta q_z = 0.038 \, \text{Å}^{-1}$. Interference fringes arising from the 91 nm top SiGe layer have reciprocal space separation of $0.007 \, \text{Å}^{-1}$ and thus appear superimposed on the strained-Si QW diffraction pattern in Fig. 1(c). The 10 nm thick strained-Si QW produces much more widely spaced thickness fringes separated by $0.063 \, \text{Å}^{-1}$, apparent as a gradual variation of the scattered intensity across the entire width of Fig. 1(c).

Coherent diffraction simulation methods were used to gain more precise insight into the nanobeam diffraction patterns. Coherent diffraction patterns were simulated using a further development of the methods described by Ying *et al.* to allow more complex heterostructures to be considered at arbitrary x-ray incident angles.[13] The simulation procedure consists of calculating the wavefield of the focused x-ray beam produced by the zone plate, computing the wavefield resulting from kinematic diffraction at the sample, and propagating the scattered beam to the detector.

The wavefield of the focused x-ray beam was computed by imprinting the phase imparted by the zone plate onto an incident x-ray plane wave and by propagating the wavefield to the sample using Fraunhofer diffraction.[13] The simulation was based on zone plate parameters matching the experimental conditions. The Fresnel zone plate was modeled using a binary approximation with Au zones, an outermost zone width of 30 nm, thickness of 400 nm, and diameter of 160 μm. The focal length for this model zone plate at 10 keV was 39 mm, matching the experiment. Simulations assumed a perfectly monochromatic beam and thus did not take into account the finite energy bandwidth of the monochromator. The simulated center stop consisted of an Au cylinder with a diameter of 60 μm and a thickness of 70 μm. The simulated order sorting aperture consisted of a circular aperture with a diameter of 30 μm located 4 mm from the focus. The amplitude outside the aperture of the OSA was set to zero. The intensity of the focused wavefield produced using this approach is plotted in Fig. 1(d), yielding a focal spot diameter of 40 nm FWHM. The distribution of intensity is similar to the report by Ying *et al.*[13] and to other previous reports.[15,16]

The relationship between the incident and scattered beams was determined by summing the amplitude of radiation scattered by each plane of atoms in the sample. Absorption and multiple scattering were neglected. The amplitude of the scattered beam was simulated by computing the lattice sum of the sample in a coordinate system consistent with its orientation and using the kinematic approximation. X-ray absorption in the heterostructure can be safely neglected because the SiGe and Si layers are much thinner than the x-ray attenuation lengths in these materials at the experimental photon energy, which are 109 μm and 134 μm, respectively. The lattice of thin films is effectively infinite in the in-plane directions, so the lattice sums along those directions can be replaced with delta functions. For the out-of-plane direction close to the surface normal, the lattice sum for one of the component layers (e.g., the 10 nm Si QW) of a multilayer thin film was computed using

$$S_1(Q_z) = F_1(Q_z) \sum_{n=0}^{N_1-1} e^{iQ_z(a_1 n + z_1)}.$$

Here, F_1 is the structure factor of an individual unit cell, N_1 is the number of unit cells in the out-of-plane z direction composing this layer, Q_z is the scattering wavevector along z, a_1 is the lattice parameter along this direction, and z_1 is the overall vertical location of the bottom unit cell within the stack of layers within the heterostructure, which is an important consideration when multiple layers are considered. The sum for the first component layer becomes

$$S_1(Q_z) = F_1(Q_z) \frac{\sin \frac{1}{2} Q_z N_1 a_1}{\sin \frac{1}{2} Q_z a_1} e^{\frac{iQ_z}{2}((N_1-1)a_1 + 2z_1)}.$$

With the addition of a second layer with structure factor F_2, number of unit cells N_2, and lattice parameter a_2 at location z_2, the total lattice sum is

$$S_{1+2}(Q_z) = F_1(Q_z) \frac{\sin \frac{1}{2} Q_z N_1 a_1}{\sin \frac{1}{2} Q_z a_1} e^{\frac{iQ_z}{2}((N_1-1)a_1 + 2z_1)}$$
$$+ F_2(Q_z) \frac{\sin \frac{1}{2} Q_z N_2 a_2}{\sin \frac{1}{2} Q_z a_2} e^{\frac{iQ_z}{2}((N_2-1)a_2 + 2z_2)}.$$

This approach is sufficiently general to be applied to an arbitrary number of layers of different crystal structure, compositions, and thickness for thin film type structures provided that the total thickness is far less than both the x-ray absorption length and the dynamical diffraction extinction depth. The assumption that multiple scattering and absorption can be neglected is valid for the small thicknesses of the Si and SiGe layers in the present study, and the range of Q considered is sufficiently narrow that the atomic scattering factor incorporated within $F(Q)$, is treated as a constant. The lattice sum is evaluated at the Q values calculated from the simulated wavefield of the focused beam after the coordinate frame is rotated to the desired diffraction geometry by the rotation matrix

$$T_i = \begin{bmatrix} \sin\theta & 0 & \cos\theta \\ 0 & 1 & 0 \\ -\cos\theta & 0 & \sin\theta \end{bmatrix}.$$

The coordinate frame is rotated to the detector by the rotation matrix

$$T_d = \begin{bmatrix} \sin(\theta - 2\theta_B) & 0 & \cos(\theta - 2\theta_B) \\ 0 & 1 & 0 \\ -\cos(\theta - 2\theta_B) & 0 & \sin(\theta - 2\theta_B) \end{bmatrix}.$$

Here, the x-axis is in the scattering plane along a radial direction with respect to the optical axis, the z-axis is along the direction of propagation of the focused x-ray beam, θ is the incident angle of the center of the incoming x-ray beam, θ_B is the Bragg angle, and the origin is at the focus. These matrices are valid for symmetric, out of plane geometries but could be generalized to allow for arbitrary diffraction conditions.

The simulations described here consider only the 91 nm thick SiGe layer and 10 nm thick strained-Si QW layer, as

illustrated in Fig. 2(a). The 300 nm thick bottom SiGe layer can be neglected because the interface between the 300 nm SiGe and the graded SiGe is too rough to have a well-defined sharp boundary, and interference fringes from these layers are absent from the experimental detector images. The total experimentally observed intensity of the SiGe reflection may, however, include a contribution from the bottom SiGe layer and thus will not be accurately simulated by this two-layer model. The deeper, graded SiGe layer had a wide range of orientations over a total mosaicity of 0.5° resulting from the plastic relaxation process and did not produce a rod of scattering aligned with the quantum well and capping layer. Similarly, diffraction from the Si substrate and the Si substrate crystal truncation rod was at sufficiently different orientations that the substrate could be neglected in the simulation. The out-of-plane lattice parameters for Si and SiGe were $a_1 = 5.387$ Å and $a_2 = 5.472$ Å, respectively. With these values, the square magnitude of the lattice sum produced is shown in Fig. 2(b), plotted as a function of incident x-ray
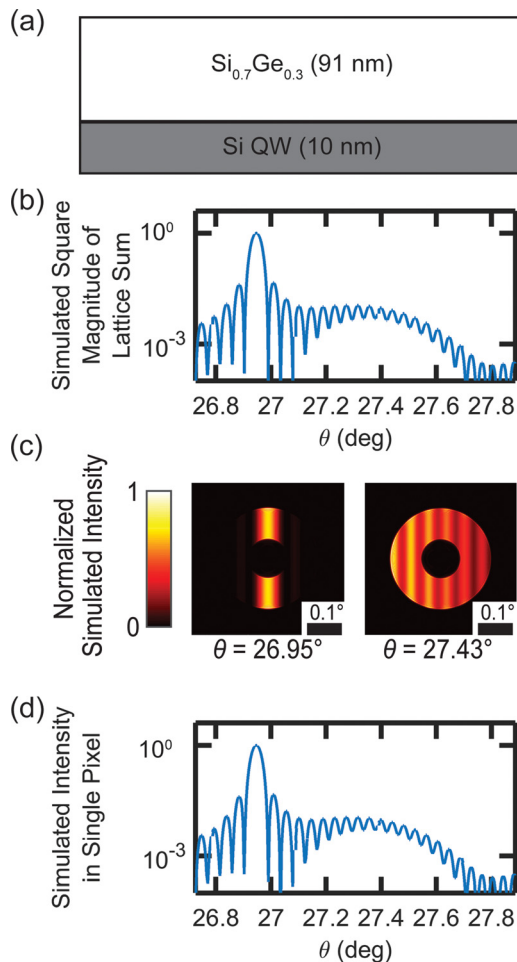
angle θ, with $Q_z = \frac{4\pi}{\lambda}\sin\theta$, as would be appropriate for plane-wave illumination.

The lattice sum was rotated into a coordinate system by the incident x-ray angle θ, which allowed the scattered amplitudes to be calculated. Simulated diffraction patterns were produced by propagating the scattered beam to the plane of the detector and recording the square magnitude of the electric field. Images produced in this way are shown in Fig. 2(c) for incident angle $\theta = 26.95°$, an angle corresponding to the most intense scattering from the 91 nm SiGe layer, and $\theta = 27.43°$, corresponding to the strained-Si QW layer. The distribution of intensity within the images qualitatively appears to be similar to the intensity distribution along the Q_z direction of the lattice sum. This intensity distribution will be systematically compared to the experimental results below.

The correspondence between the lattice sum and the simulated diffraction pattern can also be confirmed by calculating the intensity falling within an angular range corresponding to a single pixel of the x-ray detector used in the experiment. A simulated θ-2θ scan produced by computing the intensity scattered into a single-pixel-wide region of the simulated detector is shown in Fig. 2(d). Intensity features significantly narrower than the total angular range of the zone plate can be simulated accurately as shown by comparing Figs. 2(b) and 2(d). The key result of Figs. 2(b) and 2(d) is that high-resolution diffraction patterns can be experimentally extracted from experiments with highly divergent coherent x-ray beams, and that these patterns can be subsequently compared with lattice-sum simulations.

The simplest comparison between the simulation and the nanobeam diffraction data can be obtained by integrating the scattered intensity over the entire angular range spanned by the zone plate divergence. Simulated and experimentally acquired θ-2θ scans produced in this way appear in Fig. 3. The analysis

FIG. 2. (a) Schematic of the model sample used to create the simulated diffraction pattern. (b) Simulated θ-2θ diffraction pattern created using the lattice sum of the model. The reflections centered at 26.95° and 27.45° arise from the SiGe and strained-Si QW layers, respectively. (c) Simulated diffraction patterns for x-ray incident angles of $\theta = 26.95°$ and $\theta = 27.43°$. Detector images in part (c) are each normalized to the maximum intensity in each image. (d) Simulated θ-2θ scan produced by integrating the diffracted intensity in the wave-field simulation over the area of a single pixel of the two dimensional detector.
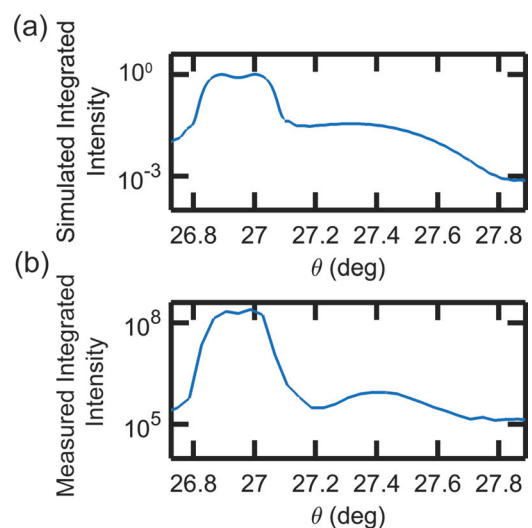

FIG. 3. (a) Simulated θ-2θ scan produced by a wave field simulation of the focused beam that has been integrated to include all of the intensity provided by the focusing optics. (b) Measured θ-2θ scan produced by integrating the intensity over an area greater than the whole image of the zone plate on the detector. The angular resolution is set by the width of the zone plate, which broadens the narrow SiGe peak and eliminated the narrow thickness fringes.

presented in Fig. 3, however, does not take advantage of the high degree of coherence of the focused x-ray beam and thus does not allow the structural features producing high spatial frequency features in the diffraction pattern to be resolved. The interference fringes arising from the 91 nm SiGe layer, for example, are absent from Fig. 3 because range of wavevectors spanned by the zone plate convergence angular width, $\Delta q_z = 0.038\,\text{Å}^{-1}$, is greater than the spacing between the SiGe fringes, $\Delta q_z = 0.007\,\text{Å}^{-1}$. At incident angles near the SiGe peak at $\theta = 26.95°$, the sharp SiGe reflection appears throughout the range of angles subtended by the zone plate and the integrated intensity across the entire zone plate is approximately constant. The simulated SiGe reflection in Fig. 3(a) thus has the angular width expected from the divergence of the zone plate, $\theta = 0.24°$, rather than the intrinsic angular width set by the thickness of the SiGe layer. The dip in the intensity near the center of the SiGe peak in both simulation and experiment arises from the obstruction of the center of the zone plate by the center stop. A higher total intensity occurs when the sample is misoriented with respect to the center of the x-ray beam but at a sufficiently small angle that some portion of the divergent beam still meets the Bragg condition. The relative minimum in intensity at $\theta = 27.19°$, in the angular range between the SiGe and Si QW reflections, is less pronounced in simulated data than the experimental data in part because the simulated intensity of interference fringes depends on the lattice parameter in the interfacial unit cell of the Si/SiGe structure, which is not a parameter varied in the fits of this model to the experimental results. A small difference between the simulation and experimental data in Fig. 3 is in the intensity of the SiGe reflection, which can in the experiment likely include a contribution from the 300 nm SiGe buffer layer that was not included in the simulation. Analysis using the integration of the full angular range of the zone plate, as in Fig. 3, clearly does not capture key structural features.

More detailed structural insight can be obtained by comparing the simulated intensity distribution with the experimental diffraction patterns. A high-resolution comparison of experimentally acquired and simulated diffraction patterns is shown in Fig. 4. Fig. 4(a) shows the lattice sum prediction of a θ-2θ scan. Simulated and experimental diffraction patterns acquired in the angular region near the SiGe (004) reflection are shown in Fig. 4(b), at incident angles indicated by the blue ticks in Fig. 4(a). At the incident angle at which the center of the zone plate meets the SiGe (004) Bragg reflection, the shadow of the center stop appears at the center of the diffraction pattern. In the adjacent images, acquired at incident angles different by steps of 0.04°, a vertical stripe of intensity appears because the difference between the actual incident angle and the nominal SiGe Bragg angle is less than the divergence of the zone plate. The angular separation between the center of the zone plate and the SiGe diffracted intensity changes with varying incident angle. Note that the angular width of the central fringe of the SiGe reflection is much narrower than the zone plate divergence.

Simulated and experimentally acquired intensity distributions for incident angles near the Bragg condition of the strained-Si QW are shown in Fig. 4(c). The central image of Fig. 4(c) has an incident angle $\theta = 27.43°$, and the remaining images were acquired at 0.08° steps from this value. The thinness of the Si QW causes its intensity to be distributed across a wide range of angles, nearly matching the zone plate divergence. As the incident angle increases from values less than the nominal Bragg angle to larger values, the intensity
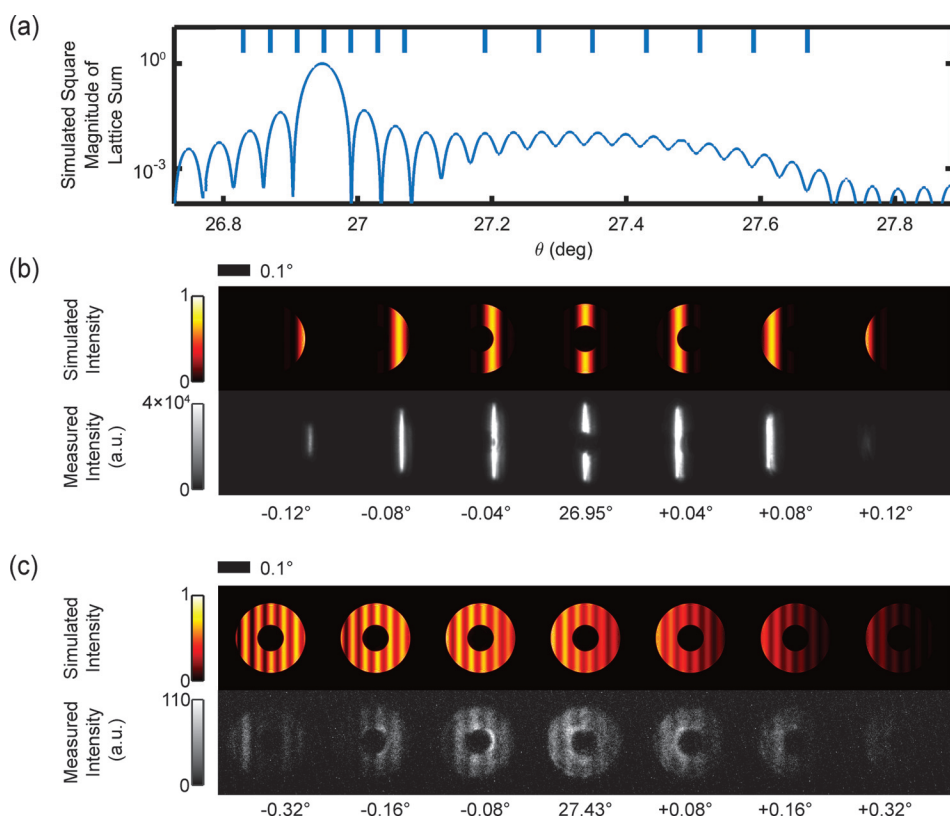

FIG. 4. (a) Simulated θ-2θ scan using the lattice sum method. Blue lines on the top axis correspond to the values of the incident angle where experimental and simulated diffraction patterns are shown below. (b) Simulated (top row) and experimental (bottom row) diffraction patterns acquired near the SiGe (004) reflection. (c) Simulated (top row) and experimental (bottom row) diffraction patterns acquired at the strained-Si QW (004) reflection.

range spanned by the images moves from the region of the intensity minimum between the SiGe peak and the strained-Si QW peak, to the strained-Si QW peak, and then to the low-intensity range at higher angles. Interference fringes from the SiGe layer appear as vertical stripes moving across diffraction patterns in Fig. 4(c).

The systematic comparison of simulated and experimental diffraction patterns can be used to extract structural information from small areas of the Si/SiGe heterostructure. Previous studies with smaller-numerical-aperture optics (and thus smaller beam divergence) have shown that the orientation of the strained-Si QW varies from location to location along the surface because of the randomness in the relaxation of the SiGe layer.[22] With the higher-divergence beam presented there, the variation in the orientation of the strained-Si QW leads to variation in the intensity and angular position of the diffracted beam. The variation in the intensity of the diffracted beam is very small in the present case because the divergence of the incident x-ray beam and the high width of the strained-Si QW reflection combine to make the effective angular widths of the reflections very broad. Fig. 5(a) shows a spatial map of the integrated intensity in a region with a width of $1.5\,\mu m$, using diffraction patterns acquired with a fixed angle of $\theta = 27.49°$. The variation of the integrated intensity of the diffracted beam within the area imaged in Fig. 5(a) is extremely small, varying by 0.3%. In this case the magnitude of the variation of the orientation of the QW is much smaller than the angular width of the Bragg reflection and all locations within the

image effectively meet the Bragg condition. Changes in the total thickness across this area are similarly small.

Differences in the orientation of the Si QW lead to systematic variation in the observed diffraction patterns across the area imaged in Fig. 5(a). The nanobeam diffraction patterns shown in Fig. 5(b) correspond to the two locations indicated in Fig. 5(a). These locations are separated by 500 nm and acquired with the same incident angle, $\theta = 27.49°$. The diffracted intensity at the two locations is distributed to different angles due to the difference in the local orientation of the Si QW. The orientation of the Si QW is determined by the local orientation of the SiGe buffer layer, which exhibits variations due to the randomness of the plastic relaxation during growth.[8] The orientation of the SiGe and Si QW layers thus varies simultaneously, and the series of fringes across the Si QW due to the SiGe thickness are observed in each location.

Diffraction patterns acquired at intermediate locations between the endpoint positions, Fig. 5(b), exhibit a gradual shift of the angular location of the diffracted intensity between adjacent images. This shift indicates that the strained-Si QW lattice is gradually rotated through the difference in orientations, which is coincidentally approximately equal to angular spacing between fringes, 0.045°. The simulated diffraction patterns for these two orientations are shown in Fig. 5(c) and are in agreement with the observed intensity. The two local incident angles (measured with respect to the planes of the strained-Si QW) were 27.47° and 27.51°, respectively.

IV. CONCLUSION

The combination of nanobeam diffraction experiments with the simulation methods presented here allows key features in thin film heterostructures to be determined precisely. The synthesis of semiconductor heterostructures often results in the creation of structural defects, lattice misorientation and tilts, or interfacial atomic steps which can have an impact on the performance or stability of devices. The Si/SiGe system discussed here is, for example, a promising route to quantum devices[32] but requires further understanding the role of defects and interface features to be developed. Such features can have a negative impact on conduction band valley-splitting and can reduce device performance.[33,34] If such features can be mastered, Si and SiGe offer to allow quantum devices to be created using the low spin-orbit coupling and zero nuclear spin of Si.[35]

The results presented here demonstrate and experimentally confirm a versatile coherent diffraction modeling approach for the interpretation of far-field intensities using a highly convergent hard x-ray nanobeam. These methods provide insight into structural parameters of a wider range of heteroepitaxial materials and can be very broadly applied in cases where existing coherent diffraction methods cannot yet be applied. Beyond this Si/SiGe system and the relevant semiconducting materials, the simulation approach described here can be applied to other important heterostructures including complex oxides such as $Pb(Zr,Ti)O_3$ (PZT),[36] or ferroelectric superlattices[37] where the lattice strain
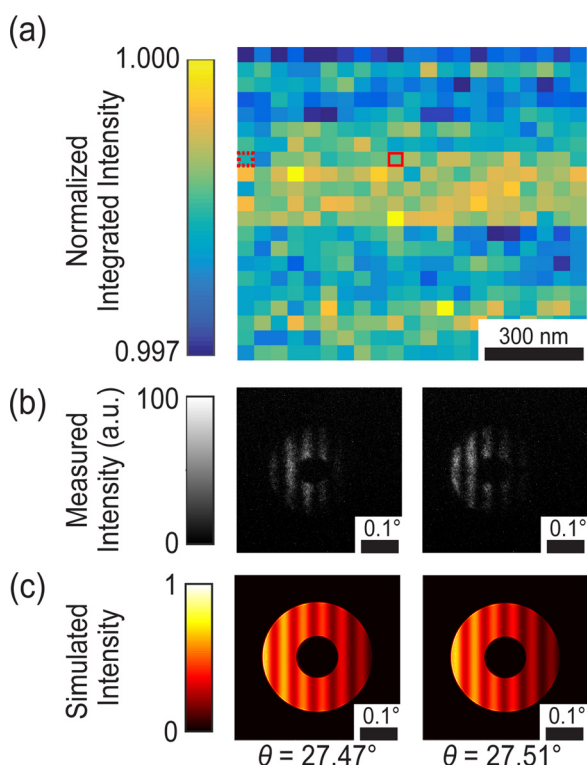

FIG. 5. (a) Map of the integrated intensity of individual diffraction patterns at a fixed incident angle. (b) Focused x-ray nanobeam diffraction patterns measured at points indicated by the dotted and solid red boxes in (a). (c) Simulated diffraction patterns for two different effective incident angles with respect to the strained-Si QW.

distribution is one among different parameters which lead to the formation of exotic polarization domains.[38] Other coherent diffraction analysis methods, including phase retrieval methods such as coherent diffraction imaging or ptychography, have so far been based on the analysis of well-defined isolated reciprocal-space distributions of the scattered x-ray intensity. When diffraction signals originating from layers with different lattice spacings significantly overlap, solving for the phase component of the crystal electron density becomes complicated. The simulations described here provide key insight when phase retrieval approaches are compromised by the presence of multiple layers with similar lattice parameters which simultaneously contribute to the intensity patterns.

ACKNOWLEDGMENTS

[1]M. A. Lutz, R. M. Feenstra, F. K. Legoues, P. M. Mooney, and J. O. Chu, Appl. Phys. Lett. **66**, 724 (1995).
[2]P. G. Evans, P. P. Rugheimer, M. G. Lagally, C. H. Lee, A. Lal, Y. Xiao, B. Lai, and Z. Cai, J. Appl. Phys. **97**, 103501 (2005).
[3]C. S. Ritz, H. J. Kim-Lee, D. M. Detert, M. M. Kelly, F. S. Flack, D. E. Savage, Z. Cai, P. G. Evans, K. T. Turner, and M. G. Lagally, New J. Phys. **12**, 103011 (2010).
[4]P. M. Mooney and J. O. Chu, Annu. Rev. Mater. Sci. **30**, 335 (2000).
[5]J. R. Watling, L. Yang, M. Borici, R. C. W. Wilkins, A. Asenov, J. R. Barker, and S. Roy, Solid-State Electron. **48**, 1337 (2004).
[6]F. A. Zwanenburg, A. S. Dzurak, A. Morello, M. Y. Simmons, L. C. L. Hollenberg, G. Klimeck, S. Rogge, S. N. Coppersmith, and M. A. Eriksson, Rev. Mod. Phys. **85**, 961 (2013).
[7]D. E. Eastman, C. B. Stagarescu, G. Xu, P. M. Mooney, J. L. Jordan-Sweet, B. Lai, and Z. Cai, Phys. Rev. Lett. **88**, 156101 (2002).
[8]P. M. Mooney, J. L. Jordan-Sweet, and S. H. Christiansen, Appl. Phys. Lett. **79**, 2363 (2001).
[9]T. Thorbeck and N. M. Zimmerman, AIP Adv. **5**, 087107 (2015).
[10]E. E. Fullerton, I. K. Schuller, H. Vanderstraeten, and Y. Bruynseraede, Phys. Rev. B **45**, 9292 (1992).
[11]U. Pietsch, V. Holy, and T. Baumbach, *High-Resolution X-Ray Scattering: From Thin Films to Lateral Nanostructures* (Springer, Berlin, 2004).
[12]S. O. Hruszkewycz, M. V. Holt, M. Allain, V. Chamard, S. M. Polvino, C. E. Murray, and P. H. Fuoss, Opt. Lett. **40**, 3241 (2015).
[13]A. Ying, B. Osting, I. C. Noyan, C. E. Murray, M. Holt, and J. Maser, J. Appl. Cryst. **43**, 587 (2010).
[14]S. O. Hruszkewycz, M. V. Holt, A. Tripathi, J. Maser, and P. H. Fuoss, Opt. Lett. **36**, 2227 (2011).
[15]H. M. Quiney, A. G. Peele, Z. Cai, D. Paterson, and K. A. Nugent, Nat. Phys. **2**, 101 (2006).
[16]F. Mastropietro, D. Carbone, A. Diaz, J. Eymery, A. Sentenac, T. H. Metzger, V. Chamard, and V. Favre-Nicolin, Opt. Express **19**, 19223 (2011).
[17]M. A. Pfeifer, G. J. Williams, I. A. Vartanyants, R. Harder, and I. K. Robinson, Nature **442**, 63 (2006).
[18]Y. Takahashi, A. Suzuki, S. Furutaku, K. Yamauchi, Y. Kohmura, and T. Ishikawa, Phys. Rev. B **87**, 121201 (2013).
[19]S. O. Hruszkewycz, M. V. Holt, C. E. Murray, J. Bruley, J. Holt, A. Tripathi, O. G. Shpyrko, I. McNulty, M. J. Highland, and P. H. Fuoss, Nano Lett. **12**, 5148 (2012).
[20]M. V. Holt, S. O. Hruszkewycz, C. E. Murray, J. R. Holt, D. M. Paskiewicz, and P. H. Fuoss, Phys. Rev. Lett. **112**, 165502 (2014).
[21]A. I. Pateras, M. Allain, P. Godard, L. Largeau, G. Patriarche, A. Talneau, K. Pantzas, M. Burghammer, A. A. Minkevich, and V. Chamard, Phys. Rev. B **92**, 205305 (2015).
[22]P. G. Evans, D. E. Savage, J. R. Prance, C. B. Simmons, M. G. Lagally, S. N. Coppersmith, M. A. Eriksson, and T. U. Schulli, Adv. Mater. **24**, 5217 (2012).
[23]J. Park, Y. Ahn, J. A. Tilka, K. C. Sampson, D. E. Savage, J. R. Prance, C. B. Simmons, M. G. Lagally, S. N. Coppersmith, M. A. Eriksson, M. V. Holt, and P. G. Evans, APL Mater. **4**, 066102 (2016).
[24]G. A. Chahine, M. H. Zoellner, M. I. Richard, S. Guha, C. Reich, P. Zaumseil, G. Capellini, T. Schroeder, and T. U. Schulli, Appl. Phys. Lett. **106**, 071902 (2015).
[25]M.-I. Richard, M. H. Zoellner, G. A. Chahine, P. Zaumseil, G. Capellini, M. Haeberlen, P. Storck, T. U. Schulli, and T. Schroeder, ACS Appl. Mater. Interfaces **7**, 26696 (2015).
[26]G. A. Chahine, M.-I. Richard, R. A. Homs-Regojo, T. N. Tran-Caliste, D. Carbone, V. L. R. Jaques, R. Grifone, P. Boesecke, J. Katzer, I. Costina, H. Djazouli, T. Schroeder, and T. U. Schulli, J. Appl. Cryst. **47**, 762 (2014).
[27]M. H. Zoellner, M.-I. Richard, G. A. Chahine, P. Zaumseil, C. Reich, G. Capellini, F. Montalenti, A. Marzegalli, Y.-H. Xie, T. U. Schulli, M. Haeberlen, P. Storck, and T. Schroeder, ACS Appl. Mater. Interfaces **7**, 9031 (2015).
[28]L. A. B. Marcal, M. I. Richard, R. Magalhaes-Paniago, F. Cavallo, M. G. Lagally, O. G. Schmidt, T. U. Schulli, C. Deneke, and A. Malachias, Appl. Phys. Lett. **106**, 151905 (2015).
[29]P. G. Evans, D. S. Tinberg, M. M. Roberts, M. G. Lagally, Y. Xiao, B. Lai, and Z. Cai, Appl. Phys. Lett. **87**, 073112 (2005).
[30]D. M. Paskiewicz, S. A. Scott, D. E. Savage, G. K. Celler, and M. G. Lagally, ACS Nano **5**, 5532 (2011).
[31]V. Mondiali, M. Bollani, S. Cecchi, M.-I. Richard, T. Schulli, G. Chahine, and D. Chrastina, Appl. Phys. Lett. **104**, 021918 (2014).
[32]P. W. Deelman, L. F. Edge, and C. A. Jackson, MRS Bull. **41**, 224 (2016).
[33]S. Goswami, K. A. Slinker, M. Friesen, L. M. McGuire, J. L. Truitt, C. Tahan, L. J. Klein, J. O. Chu, P. M. Mooney, D. W. van der Weide, R. Joynt, S. N. Coppersmith, and M. A. Eriksson, Nat. Phys. **3**, 41 (2007).
[34]M. Friesen, M. A. Eriksson, and S. N. Coppersmith, Appl. Phys. Lett. **89**, 202106 (2006).
[35]J. J. L. Morton, D. R. McCamey, M. A. Eriksson, and S. A. Lyon, Nature **479**, 345 (2011).
[36]J. Y. Jo, P. Chen, R. J. Sichel, S. H. Baek, R. T. Smith, N. Balke, S. V. Kalinin, M. V. Holt, J. Maser, K. Evans-Lutterodt, C. B. Eom, and P. G. Evans, Nano Lett. **11**, 3080 (2011).
[37]P. Zubko, N. Jecklin, A. Torres-Pardo, P. Aguado-Puente, A. Gloter, C. Lichtensteiger, J. Junquera, O. Stephan, and J. M. Triscone, Nano Lett. **12**, 2846 (2012).
[38]A. K. Yadav, C. T. Nelson, S. L. Hsu, Z. Hong, J. D. Clarkson, C. M. Schlepüetz, A. R. Damodaran, P. Shafer, E. Arenholz, L. R. Dedon, D. Chen, A. Vishwanath, A. M. Minor, L. Q. Chen, J. F. Scott, L. W. Martin, and R. Ramesh, Nature **530**, 198 (2016).